SCIENTIFIC REPORTS

OPEN

SUBJECT AREAS:
APPLIED PHYSICS
NANOWIRES
NANOPARTICLES
ULTRAFAST PHOTONICS

Received
6 February 2013

Accepted
24 May 2013

Published
13 June 2013

Correspondence and requests for materials should be addressed to M.-H.C. (mh.cho@yonsei.ac.kr) or C.K. (iron74@gist.ac.kr)

Strongly Enhanced THz Emission caused by Localized Surface Charges in Semiconducting Germanium Nanowires

Woo-Jung Lee[1], Jin Won Ma[1], Jung Min Bae[1], Kwang-Sik Jeong[1], Mann-Ho Cho[1], Chul Kang[2] & Jung-Sub Wi[3]

[1]Department of Physics and Applied Physics, Yonsei University, Seoul 120-749, Korea, [2]Advanced Photonics Research Institute, Gwangju Institute of Science and Technology, Gwangju, 500-712, Korea, [3]Division of Convergence Technology, Korea Research Institute of Standards and Science, Daejeon 305-340, Korea.

A principal cause of THz emission in semiconductor nanostructures is deeply involved with geometry, which stimulates the utilization of indirect bandgap semiconductors for THz applications. To date, applications for optoelectronic devices, such as emitters and detectors, using THz radiation have focused only on direct bandgap materials. This paper reports the first observation of strongly enhanced THz emission from Germanium nanowires (Ge NWs). The origin of THz generation from Ge NWs can be interpreted using two terms: high photoexcited electron-hole carriers (Δn) and strong built-in electric field (E_b) at the wire surface based on the relation $E_{THz} \propto \partial J/\partial t$. The first is related to the extensive surface area needed to trigger an irradiated photon due to high aspect ratio. The second corresponds to the variation of Fermi-level determined by confined surface charges. Moreover, the carrier dynamics of optically excited electrons and holes give rise to phonon emission according to the THz region.

In recent years, improvement in the various fields of THz research has been achieved with the development of an advanced laser source with femtosecond (*fs*) pulses[1–3]. The observation of THz waves between the microwave and infrared regions has motivated further expansion in research directions not previously considered, such as carrier dynamics with ~*ps* lifetimes and applications in biomedical research using extremely low energy (~ meV). In particular, the radiation of THz waves from semiconductors is of interest as an optical source because utilizing the surface depletion field rather than an applied bias voltage method (with a photoconductive antenna, PCA) is easy and simple. In a PCA, analysis requires consideration of antenna response and semiconductor–electrode interfaces. Currently, unbiased THz emissions from a variety of semiconductors have been observed in materials including InAs, GaAs, GaSb, InSb, and InP[4–9]. According to the published literature, it is generally accepted that the THz wave emitted from the semiconductor results from an ultrafast charge transport such as photocurrent surge in surface field, dynamic Dember effect, plasma oscillations, and nonlinear optical rectification (OR) near the surface[10,11].

In addition, an intense THz pulse can be emitted from the nanostructure semiconductors mentioned previously[12–16]. The choice of material for a suitable THz emitter is determined by several properties, including high absorption, greater electron and hole mobility, fast recombination rates, short carrier lifetimes, and appropriate bandgap values. To date, the semiconductors used for THz emission are primarily direct bandgap or compound semiconductors. However, useful features of the nanostructures, such as high aspect ratio, extensive surface area, and simple manipulation, have revived the utilization of indirect bandgap semiconductors (Si, Ge, Si-Ge alloy, etc.). For Si, several groups have observed increases of THz pulse intensity by changing the flat surface into nanostructures to enhance the absorption rate[17,18].

The present study sheds new light on Ge material, which has been undervalued as a THz optical source. Ge allows optically efficient photo current generation of e–h pairs for direct transition near the Γ point and shows faster e–h mobility and large optical absorption in the visible/near-IR range. Herein, we investigate THz emission spectroscopy of cone-shaped Ge nanowires (Ge NWs) containing Au nanoparticles on the wire sidewall as a function of wire length. As a result, a strongly enhanced THz pulse in conjunction with high absorption over a wide range of light was detected from the Ge NWs, depending on wire length. Moreover, THz pulse intensity emitted from the Ge NWs of 5 μm in length indicated an extraordinary value, even when compared with that emitted from the InAs, which are well-known as highly efficient radiators[10]. In the study of the THz generation

mechanism, interpretation of the THz wave is very difficult because both the optical wave determined by quantum transition of the electron and the electromagnetic wave explained by classical movement of the electron are not suitable in the THz wave region. Therefore, to investigate the emission characteristics caused by the mechanism of THz generation, new technologies and new tools must be developed. In this paper, we first tried to analyze the THz pulse emitted from the Ge NWs with respect to surface carrier concentration and carrier dynamics by using X-ray photoemission spectroscopy (XPS) and THz emission spectroscopy. The analysis results explain the enhanced THz pulse intensity in Ge NWs with Au nanoparticles based on the geometric effect of the extensive surface area; i.e., (i) Surface modification into tapered nanowire brings about an increase of confined surface charge, which induces an increase of Fermi-level, resulting in a strong built-in electric field. (ii) The Ge NWs groove captures the photon with multiple paths of irradiated light (*fs* pulse laser) and causes highly photoexcited e–h carriers. In our system, both Fermi-level and e–h pairs increase in proportion to the wire length. (iii) Consequently, photoexcited e–h pairs are accelerated by the strong built-in field, and the subsequent transient current generates the THz wave.

These results provide new insight into the application of Ge NWs, which is unlike that of Ge wafers, and they suggest the potential for the use of Ge NWs as an alternative material for optical devices such as THz emitters.

Results

Ge NWs were synthesized by using a vapor-liquid-solid (VLS) method, varying the growth time from 12 to 80 min while keeping other process parameters constant **(see Methods)**. As process time increased, the wire length increased, and the wire density per unit area decreased **(Supplementary Fig. S1)**. In this system, the Ge NWs were grown to a tapered shape with a steeple-crowned apex with an Au tip, and a Ge buffer layer was formed on the Si substrate in proportion to growth time, as shown in the SEM images of Figs. 1a to 1c. Such geometric characteristics stem from the ease of depositing Ge atoms radially on the sidewall of the wire by the chemical vapor deposition (CVD) process. In general, the CVD process occurs vertically simultaneous with VLS growth through an Au catalyst in the Ge wire, the tapered shape of the Ge NWs[19,20]. For a more detailed examination, TEM measurements were made on each individual Ge NW. Figure 1d clearly shows the tapered shape of the Ge NWs suspended on the TEM mesh grid. The Ge NWs were grown into a perfect single crystal structure with a thin Ge oxide layer **(Supplementary Fig. S2)**. In this system, Au diffusion from the tip of the wire was observed, as shown in Figs. 1e to 1g and Fig. S2. This phenomenon induces surface modulation of the Ge NWs by entirely covering the external wire surface with Au nanoparticles (2–3 nm size). The morphological properties of the Ge NWs, including length, diameter, and growth rate, are described in detail in Supplementary Figs. S1 and S2.

The THz pulse emitted from the Ge NWs was measured using THz emission spectroscopy, as shown in Fig. 2a. After irradiation of a *fs* pulse laser from a Ti:sapphire, THz pulses that radiated from the Ge NWs as a function of wire length were detected, as shown in Fig. 2b. Interestingly, the THz pulse intensity was drastically increased at 2.9 μm in length and maximized at 5.2 μm in length. Figure 2c shows frequency spectra corresponding to the THz pulses of Fig. 2b, in which emission peaks occur mainly at 0.2 THz. The peak-to-peak values of the THz pulse intensity, extracted from Fig. 2b, are plotted in the graph of Fig. 2d. This result implies that Ge NWs can be used for high-performing THz emitters that depend on wire length. To verify the potential of Ge NWs as alternative THz emitters, a comparative experiment of THz pulse intensity was performed between Ge NWs 5 μm in length and *n*-InAs (1×10^{16} cm^{-3}) and *n*-GaAs (1×10^{17} cm^{-3}) wafers, which are the materials currently used as highly efficient radiators. To clearly extract the effect of Ge NWs, *n*/*i*-Ge wafers (1×10^{13} cm^{-3}/1×10^{15} cm^{-3}) were also measured. The THz pulses and the frequency spectra obtained from these materials are shown in Fig. 3a and 3b, respectively. According to previous research, the Ge wafer has been shown to rarely emit THz pulses; the values of THz pulse intensities in *n*-InAs and *n*-GaAs wafers were 5 times and 17 times greater than that in Ge wafer, respectively[10]. However, in contrast to Ge wafer, Ge NWs have

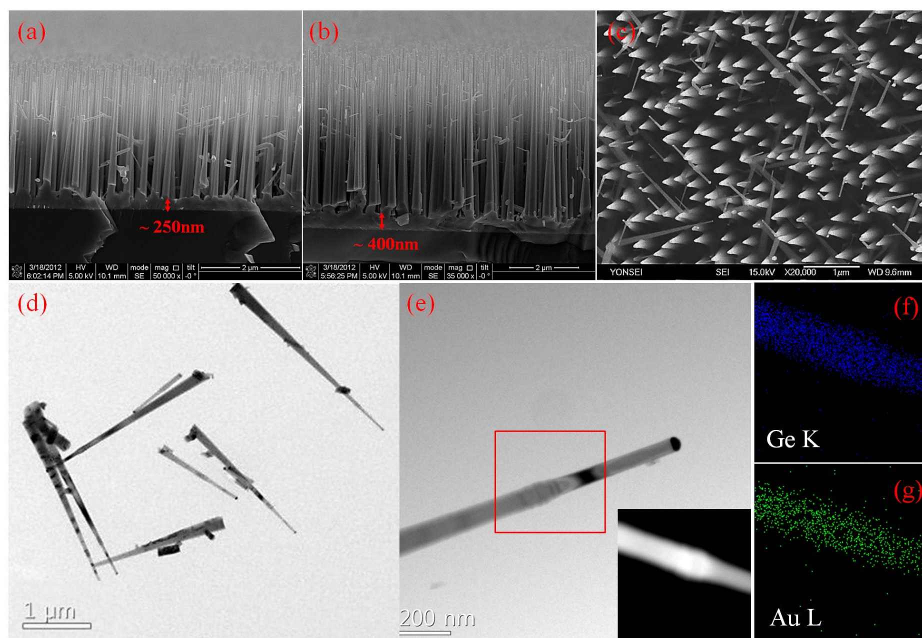

Figure 1 | A representative SEM image of Ge NWs in a vertical view after a growth time of 40 min (a) and 60 min (b). (c) SEM image of (b) in the top view, showing that most Ge NWs were vertically grown against a Si (111) wafer with a thick Ge buffer layer. (d) and (e) show low- and high-magnified TEM images of (b). The Ge NWs became tapered due to the CVD growth on the sidewall. The diffusion of Au from the tip at the top of the wire is shown in the EDX results of (f) and (g), extracted from the red rectangle region in (e).

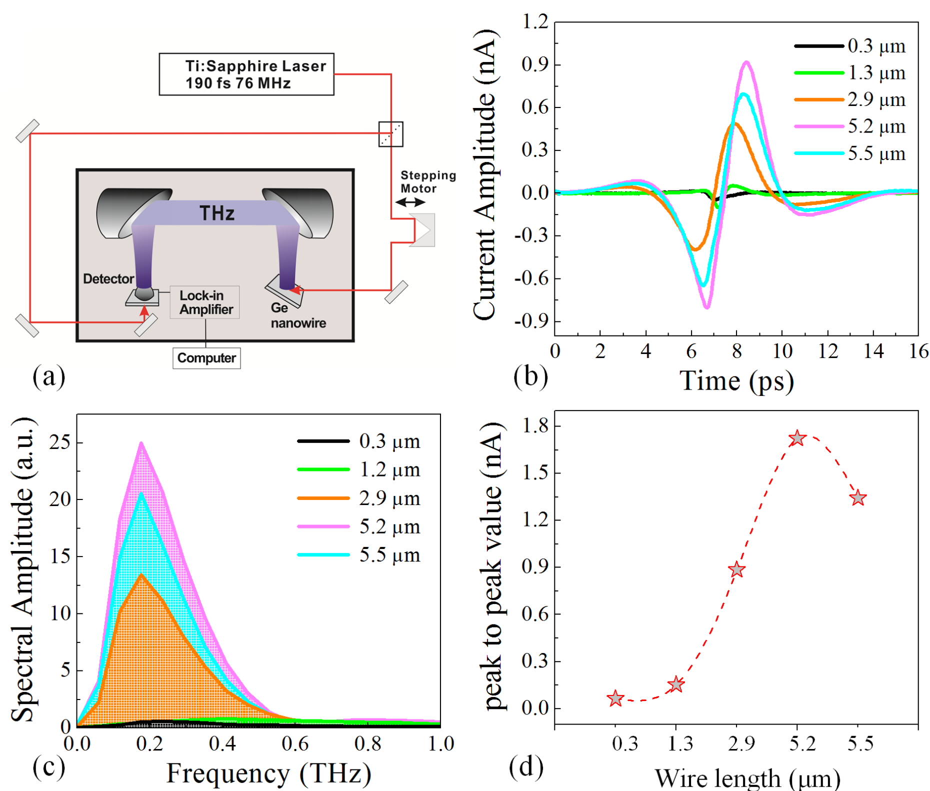

Figure 2 | (a) A schematic diagram of the experimental setup used for the THz emission. (b) The THz pulse generated from the Ge NWs as a function of wire length. (c) Fast-Fourier-Transform (FFT) frequency spectra corresponding to the THz pulse displayed in (b). (d) The graph obtained from the peak-to-peak values of the THz pulse as a function of wire length in (b).

demonstrated incredible efficiency as THz emitter; comparisons are shown in Fig. 3c. Setting the peak-to-peak value of the *n*-InAs THz pulse as unity to act as a reference, the THz pulse of the Ge NW was about 2 times greater than that of the *n*-GaAs and nearly the same as that of the *n*-InAs. This is a very compelling feature in comparison with the Ge wafer.

Primarily, THz emission from the Ge surface arises due to either charge separation by the built-in electric field or difference in the diffusion coefficients between electron and hole (photo-Dember effect). THz emission by OR mechanism depends on crystallographic orientation of the sample or azimuthal angle of the incident light, an effect which is mainly observed in ZnTe or III-V materials, not in Ge NWs[21,22]. Thus, we consider the two cases of built-in electric field and photo-Dember effect. In the case of the former, GaAs is a suitable material, generating a THz wave by a built-in electric field because GaAs has a larger bandgap and higher surface field. The polarity of the THz wave can be controlled using *n*- and *p*-type GaAs, which has been verified in experiments[23]. In the case of the latter, InAs is an appropriate material for THz generation using the photo-Dember field due to its high electron mobility (40,000 $cm^2V^{-1}s^{-1}$). Even if no built-in, or only a weak built-in, electric field exists, the different diffusion speeds between electrons and holes lead to a charge separation and induce a photo-Dember field, resulting in generation of a THz wave. Therefore, THz pulses from n- and p-type InAs have the same polarity[23]. The polarity of a THz pulse generated from the semiconductor is considered as a criterion to distinguish the THz generation mechanism between built-in field and photo-Dember field. For Ge NWs, the THz pulse shows different polarity depending

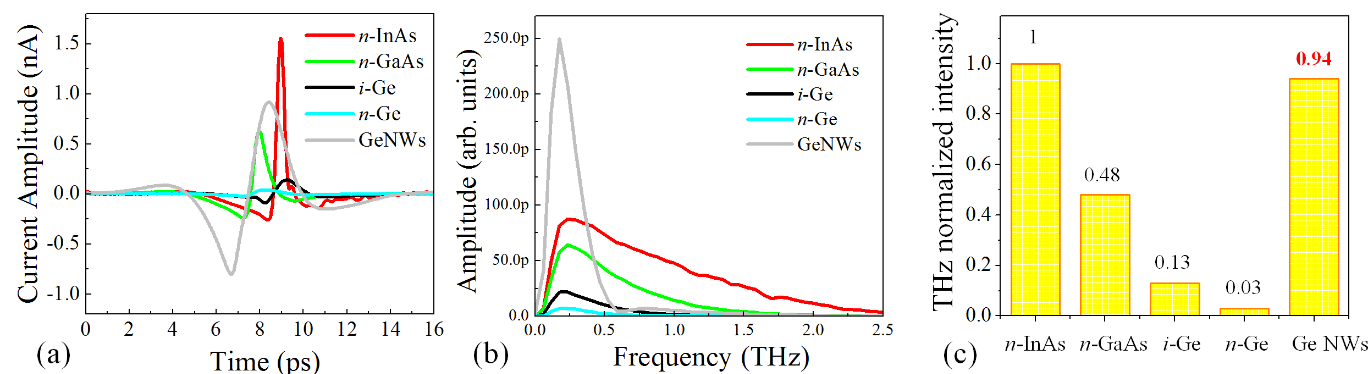

Figure 3 | (a) THz pulses emitted from various semiconductors, such as *n*-InAs, *n*-GaAs, *i*-Ge, *n*-Ge, and Ge NWs by the Ti:sapphire *fs* pulse laser under identical conditions. (b) FFT frequency spectra corresponding to the THz pulse displayed in (a). (c) The histogram extracted from the peak-to-peak values of the THz pulse in (a).

on wire length, which implies that THz generation from the Ge NWs is caused by a built-in electric field. Additionally, Ge has neither a higher mobility nor a narrower bandgap than InAs.

THz pulse generation at the semiconductor surface depends on the physical motion of the optically excited e–h carriers that were spatially separated by the built-in electric field induced by the depletion region at the Ge wire surface, resulting in a transient photocurrent($J(t)$) varying on a sub-picosecond time scale, given by $E_{THz} \propto \partial J/\partial t$. The photocurrent is defined as $J(t) = e\mu\Delta n E_b$, where E_b is the built-in electric field at the surface, μ is the carrier mobility, and Δn is the photoexcited e–h carriers; i.e., from the equation $E_{THz} \propto \frac{\partial n(t)}{\partial t} e\mu E_b$, E_b and Δn become important variables for THz generation from the Ge NWs. Analysis of the THz pulse generated from the semiconductor surface can help in understanding the materials themselves because the shape of the THz pulse measured by THz emission spectroscopy can be determined by rapidly varying $J(t)$ in E_b, which provides information about the carrier dynamics.

First, $J(t)$ was calculated, as shown in Figs. 4a and 4b, by integrating the radiated THz pulses of Fig. 2b because their shape and area represent carrier dynamics and the number of photogenerated carriers, respectively. As shown in the $J(t)$ graphs, the quantity of photogenerated carriers was significantly increased to more than were present in the Ge NWs of 2.9 μm in length. Another feature is that J(t) was negative in Ge NWs greater than 1.3 μm in length, which means that the dominant carrier type changed depending on wire length; i.e., electrons became the dominant carrier in Ge NWs greater than 1.3 μm in length, which corresponds to the change of the THz pulse polarity. Since an increase of $J(t)$ is related to Δn, the absorbance of the Ge NWs was measured (Fig. 5). Similar to the $J(t)$ tendency, the absorbance spectra indicated an abrupt increase of absorption in the Ge NWs of 2.9 μm in length and greater. This saturation phenomenon could be explained through skin effects given by $\delta = \left(\frac{2}{\sigma_0 w \mu_0}\right)^{1/2}$. In the case of Ge materials, calculated skin depth (δ) was about 2.9 μm when a photon energy of 1.5 eV (790 nm) was irradiated onto the sample, which agreed with our absorbance spectra. The inset of Fig. 5 shows a photograph of the Ge NWs samples of 5.2 μm and 5.5 μm in length under white light illumination. As the Ge NWs length increased, the color changed from a mirror-like to a black-colored surface. It has been reported that the black color is caused by the geometric impact of the cone-shaped nanowires, resulting in an effective suppression of the reflection and perfect absorption of nearly 100% in the visible and near-IR spectra (**Supplementary Fig. S3**)[24]. On the other hand, unlike the saturated absorbance spectra, the quantity of photoexcited carriers generating the THz pulse is still increased in Ge NWs greater than 2.9 μm.

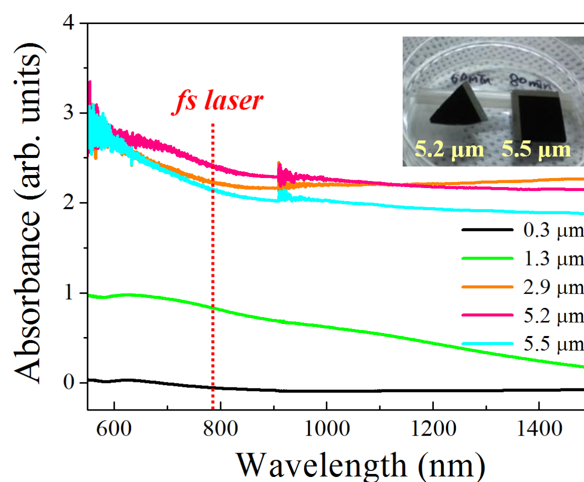

Figure 5 | Absorbance spectra of the Ge NWs depending on the wire length in the Vis-NIR region. The saturated absorbance was observed in Ge NWs greater than 2.9 μm length at a Ti:sapphire photon energy of 790 nm. Inset shows a photograph of the Ge NWs sample grown vertically with a cone shape of 5.2 and 5.5 μm in length, indicated by the color black.

Next, the E_b formed at the Ge NWs surface was considered, because $J(t)$ depends on both Δn and E_b. Most semiconductors have an E_b at the surface, which is induced by bending of energy bands beneath the surface due to the difference in Fermi-level between the surface state and bulk material. Considering *n*-type Ge, as depicted in Fig. 6c, the Fermi-level of the *n*-type is close to the conduction band. The lower Fermi-level of the surface state compared to that of the *n*-type causes upward band-bending at the surface, resulting in an accumulation of holes and subsequent formation of the built-in electric field. The free electron rate in this layer is much lower than in the *n*-type, and this region is called the depletion layer (as indicated by the blue line in Fig. 6c). When the *fs* pulse laser is irradiated onto the *n*-type Ge, photoexcited electrons and holes are accelerated by the existing built-in electric field. They screen the surface field via electron drift into the bulk and hole drift toward the surface, even in the absence of an externally applied bias. Moreover, dipole oscillations occur until a new balance is reached, in which radiation can be estimated as a THz wave, as shown in Fig. 2b. In the case of *p*-type Ge, photoexcited electrons and holes are driven in reversed directions compared with *n*-type Ge because of the opposite polarity, as demonstrated in the THz pulse; i.e., the THz pulse can give information on the doping type of the material. According to the THz generation equation, the THz field is linearly proportional to the built-in

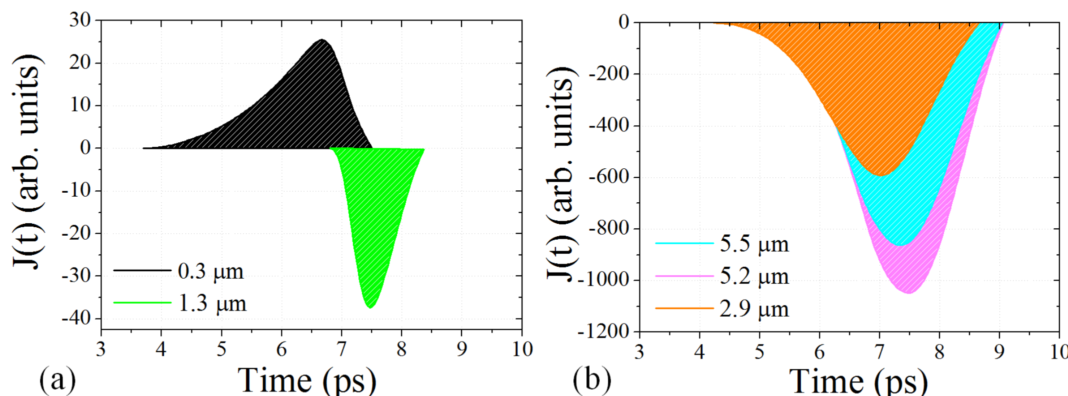

Figure 4 | The calculated photocurrent *J(t)* obtained by integrating the THz pulse of Fig. 2b in Ge NWs of 0.3 and 1.3 μm (a) and 2.9, 5.2, and 5.5 μm length (b).

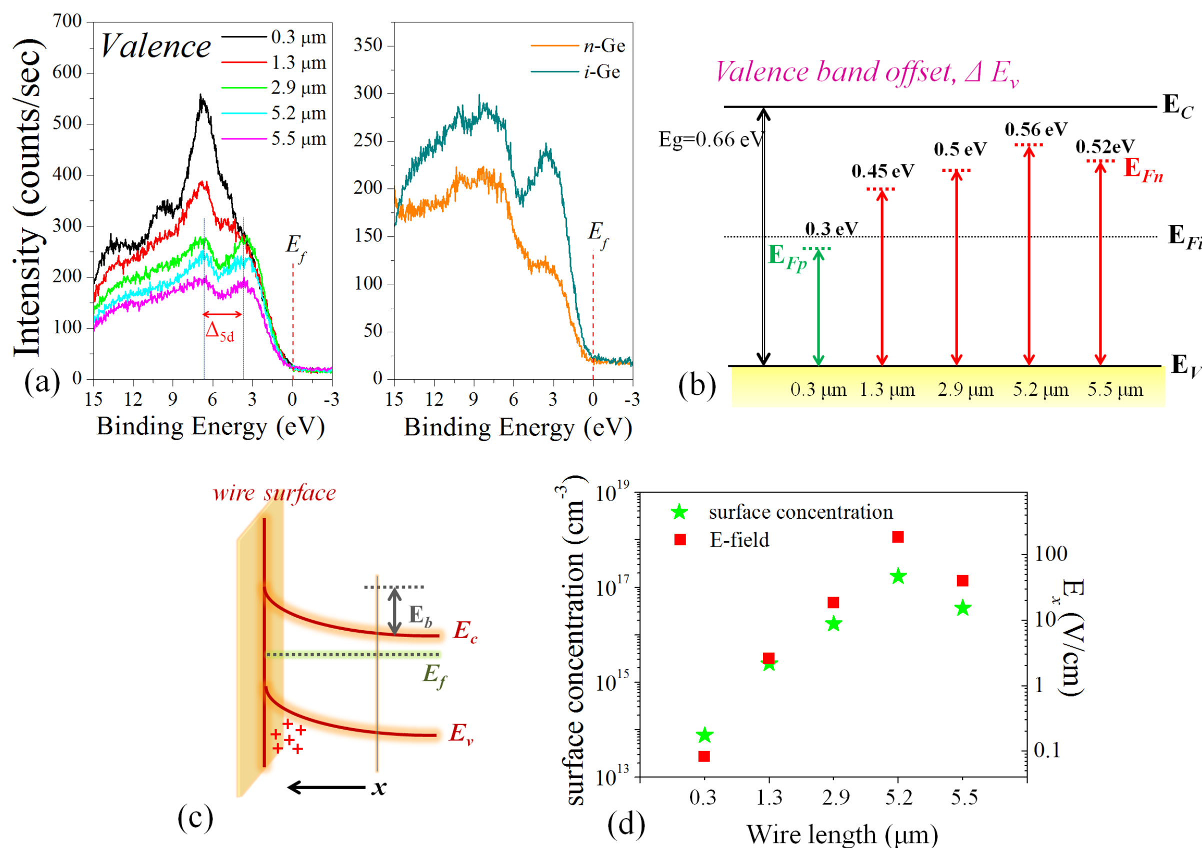

Figure 6 | (a) Valence band spectra of Ge NWs as a function of wire length, and *i*/*n*-Ge wafers measured by XPS. (b) Schematic diagram of band structure indicating the valence band offset (ΔE_v), which was extracted from the valence band of (a). (c) Modeling of a gradient of E_F depending on distributional characteristics, which are applied in an n-type Ge NWs from 1.3 to 5.5 µm. (d) Calculated values of the built-in electric field (E_b) formed in the Ge NWs as a function of wire length.

electric field, which means that an increase of the built-in electric field leads to a stronger THz pulse. As an effective method for enhanced THz pulses, an increase of Fermi-level is determined between the surface state and the bulk state, causing an increase of the surface field. Based on the above factors, the Fermi-level and surface carrier concentration are investigated by using the XPS tool, since it is well known to be surface sensitive. An induced electric dipole is generally normal to the surface, and the strength is determined by the surface carrier concentration. Considering the surface-to-volume ratio in the nanowires, the exposed surface area is significantly larger than the wafer, which therefore attracts a large number of carriers to the Ge NWs in proportion to the increase in the surface area. To obtain the carrier concentration and Fermi energy at the wire surface, the valence band spectra of the Ge NWs as a function of wire length were measured using XPS, which provided information on the charge distribution at the Fermi edge of the Ge NWs (Fig. 6a). The valence band of the *i*-Ge wafer was also measured to provide a reference sample for a more exact analysis. The valence band offsets (ΔE_v) of the Ge NWs were extracted from the normalized valence band spectra, calibrating their ΔE_v based on the ΔE_v of the *i*-Ge wafer as a standard. As ΔE_v determines the Fermi energy (E_F), the schematic diagram of the band structure is shown in Fig. 6b. There were distinctive features in the band structure; one is the E_F of the p-type character in Ge NWs with the shortest length of 0.3 µm, and the other is a slight falloff in E_F of Ge NWs with the longest length, 5.5 µm. The former gives information on carrier type, and the results were consistent with the *J(t)* of Figs. 4a and 4b. The trend presented in the latter seems to be involved in the THz pulse intensity of Fig. 2b. To comprehend this phenomenon, the exposed surface area per unit area of wafer was considered because it is geometrically proportional to the wire length and density, although X-ray was irradiated onto the same area of all samples. Based on the SEM images, the total surface area of the wires per unit area was computed approximately, which indicated similar trends to the change of E_F (**Supplementary Fig. S4**). The surface carrier concentration using E_F values extracted from the valence band was calculated using equations (1) and (2), as follows (carrier type is generally denoted by n_0 and p_0 in n-type and p-type, respectively), and their values are plotted in the graph of Fig. 6d.

$$n_0 = n_i \exp\frac{E_F - E_{Fi}}{kT} \quad (1)$$

$$p_0 = n_i \exp\frac{E_{Fi} - E_F}{kT} \quad (2)$$

Since most of the calculated surface concentrations were higher than the intrinsic carrier concentration (n_i is 2.4×10^{13} cm^{-3} in Ge), a gradient of E_F depending on the distributional characteristic of the carrier concentration toward the wire surface was modeled as illustrated in Fig. 6c. The built-in electric field (E_b) formed in Ge NWs is given by $E_x = -\left(\frac{kT}{e}\right)\frac{1}{N_d(x)}\frac{dN_d(x)}{dx}$ (**refer to Methods**), and the calculated E_b is plotted in Fig. 6d, which, interestingly, shows a similar tendency to the peak-to-peak value of the THz pulse intensity (Fig. 2d). In particular, the decrease in E_F of Ge NWs of 5.5 µm in length, in contrast to the increasing trend in the E_F of Ge NWs reaching up to 5.2 µm in length, is consistent with the decrease of the spectral amplitude of the THz spectrum. Consequentially, the THz pulse intensity was more affected by the E_b at the surface than by Δn; i.e., increased exposed surface area collecting the photons is an

important factor for THz generation by increasing E_b with a steep gradient of band bending.

In Ge NWs, even though the necessary requirements, such as high photoexcited e-h pairs and strong built-in electric field, are satisfied for THz generation, behavior of photoexcited e–h carriers moving on a picosecond scale should be considered to clarify interpretation of the THz pulse emitted from the Ge NWs. Several groups have given detailed accounts of nonequilibrium e–h carrier dynamics in Ge photoexcited by an *fs* pulse to describe a direct cause for the emission of a THz wave on the basis of theoretical calculations and experimentation[25–28]. *Bailey et al.* calculated the nonequilibrium e–h carrier dynamics of Ge when the *fs* pulse was irradiated using an ensemble Monte Carlo method[25]. From the carrier distribution calculation, it was found that e–h pairs are created near the Γ-point, and then electrons quickly scatter to the X-point within the *fs*. After that, they scatter to the lowest L-valley within a few picoseconds due to the strong intervalley phonon scattering. *Strait et al.* experimentally observed the absorbance in the THz region using optical-pump THz-probe spectroscopy and ascribed it to the intraband relaxation of e–h carriers, quoting the calculation results of *Bailey et al.*[29]. Thus, as Ge NWs have *n*-type characteristics, it is reasonable to assume that the emission of about ∼2 THz in our results is attributable to relaxation of photoexcited electrons from the X- to the L-valley, because carrier intervally phonon scattering time is about ∼5 *ps*. That is, a THz pulse can be emitted from the Ge materials. This result provides direct evidence of photoexcited carriers moving on a picosecond scale in Ge NWs and suggests that Ge NWs can be used as an intense THz nanoscale emitter with a cone-shaped nanowire.

Additionally, Au nanoparticles influence on THz generation was investigated in Ge NWs. Interestingly, as Ge NWs were entirely covered with Au nanoparticles during wire growth, we compared the THz emission from the Ge NWs with and without Au. The Au in Ge NWs was removed by immersion into an HCl-containing etch solution (9 parts by volume Transene TFA [an aqueous solution of I_2 and KI] to 1 part by volume 36% HCl) for 1 min. After that, the Ge NWs were rinsed in 1 M HCl and then dried in isopropyl alcohol for 10 s[30]. Radiated THz pulses from the Ge NWs without Au as a function of wire length were measured by the same method using THz emission spectroscopy; results are shown in Figs. 7a and 7b. The THz pulse intensity of Ge NWs without Au is significantly decreased compared with the Ge NWs with Au. To clearly render the difference of the THz pulse intensity between the absence and presence of Au, peak-to-peak values were obtained from the THz pulses of the Ge NWs with and without Au, which are plotted in the graph of Fig. 7c. An astonishing finding is that, in the case of Ge NWs without Au, THz pulse intensity gradually increased and saturated when the Ge NWs reached 2.9 μm in length. This stems from the Ge material skin depth (δ) of 2.9 μm, which is demonstrated by the absorbance spectra measured from the Ge NWs without Au (**Fig. S5 d**); the ∼3 μm in length Ge NW is perceived as a critical point to generate maximum photoexcited e–h carriers for THz emission, regardless of Au. In the case of Ge NWs without Au, to produce a built-in electric field at the wire surface, the same analysis method using XPS was employed, and results are displayed in Supplementary Figure S5. The built-in electric field was drastically decreased to below 10 V/cm without Au in Ge NWs, which also indicates a decrease of carrier concentration at the wire surface. As a consequence of this result, we apprehend that Au has a decisive effect to notably enhance THz emission in Ge NW greater than 2.9 μm in length. Since valence bands are dominantly determined by the Au *s*-band and *d*-band for Ge NWs with Au, the valence band spectra were compared between absence and presence of Au, as shown in Fig. S5a and Fig. 6a[31,32]. The spin-orbit splitting (Δ_{5d}) reflecting the Au-Au *d-d* interaction was only observed in the case of Ge NWs with Au greater than 2.9 μm in length (Fig. 6a), which can affect ΔE_v, leading to an increase of E_F. Considering the surface sensitivity of the XPS, Δ_{5d} in the valence band was ascribed not to the Au tip at the top, but to Au nanoparticles on the sidewall of the wire. In other words, Au nanoparticles play an important role in THz emission; i.e., they give rise to an increase in the surface carrier concentration in Ge NWs, which then induces an increase of E_b strength, resulting in a substantial improvement of the THz emissions. In contrast, the valence bands of Ge NWs without Au showed similar spectra, regardless of wire length, and the ΔE_v extracted from them is shown in Fig. S5a. The carrier type is changed from p-type to *n*-type Ge NWs at lengths greater than 2.9 μm, which is consistent with the change of THz pulse polarity, as shown in Fig. 7a. Surface carrier concentration was also calculated by using Eqs. (1) and (2), and their values indicated falloff ranging from $\sim 10^{13}$ to $\sim 10^{15}$ cm^{-3} (Fig. S5c), resulting in a reduction of E_b strength compared with Ge NWs with Au. In addition to the diminished THz pulse intensity, the broad frequency spectra are also examined in Ge NWs without Au, as shown in Fig. 7b. From the comparison of surface carrier concentration, we deduced which carrier between electron and hole is dominant in generating THz pulse. In Ge NWs with Au, calculated electron concentration is substantially higher ($\sim 10^{17}$ cm^{-3}, as shown Fig. 6d) than Ge NWs without Au owing to the free carriers of Au. Even though photoexcited electron-hole pairs occur, electron quantity is still higher due to the electrons of Au atoms; i.e., electron motion can predominantly determine the THz pulse shape. On the other hand, in Ge NWs without Au, photoexcited both electron and hole can affect THz emission. According to published reports, photoexcited holes in the three valence bands (heavy hole, light hole,

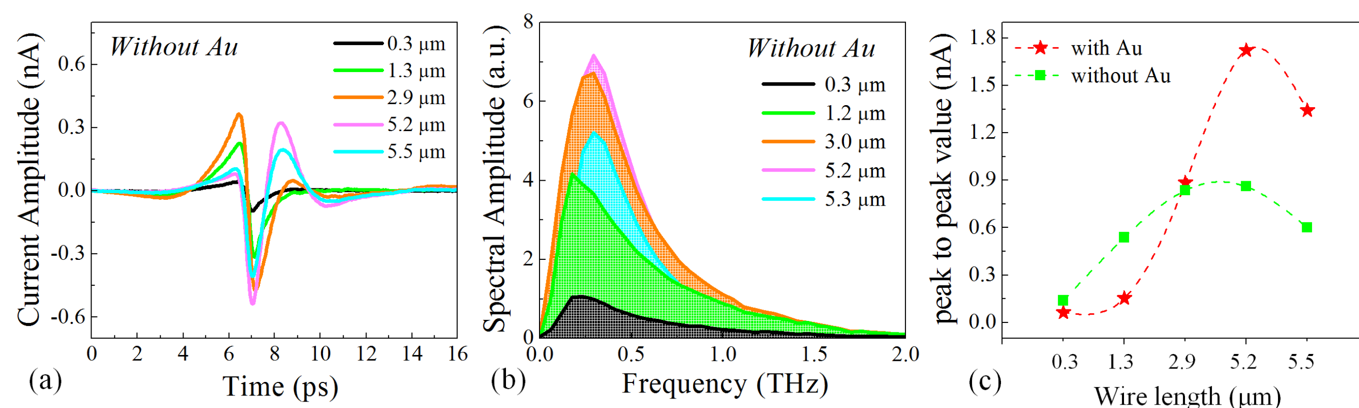

Figure 7 | (a) The THz pulse generated from the Ge NWs without Au, as a function of wire length. (b) FFT frequency spectra corresponding to the THz pulse displayed in (a). (c) The graph obtained from the peak-to-peak values of THz pulses of the Ge NWs with/without Au as a function of wire length.

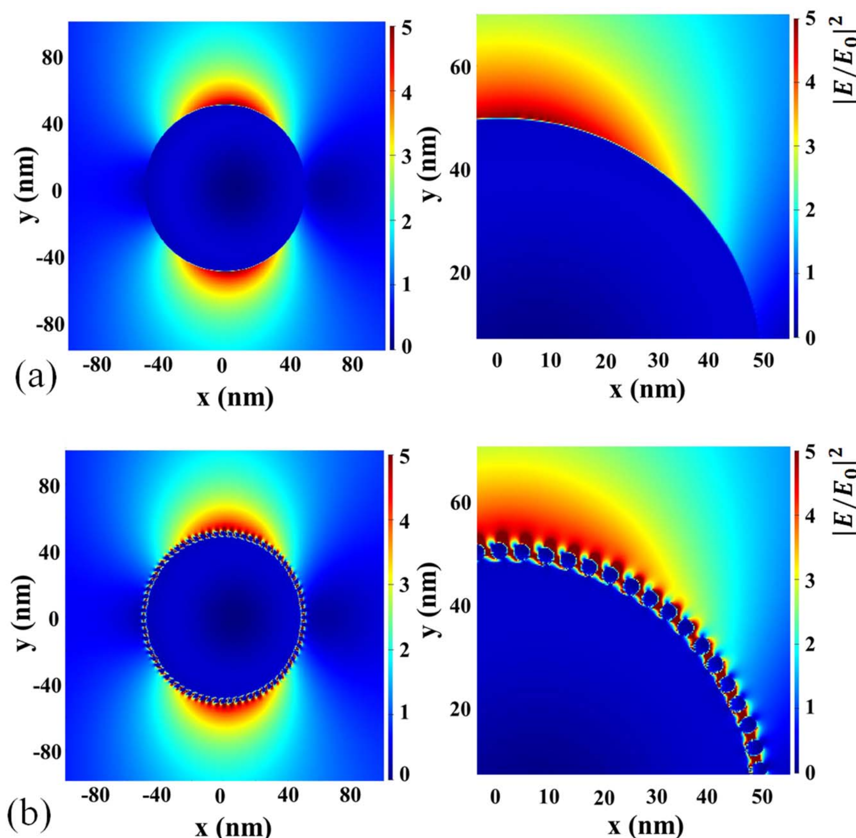

Figure 8 | The results of 2-D FDTD simulation. Squared magnitude of the local electric field amplitude of Ge NWs (a) without Au nanoparticles (b) with Au nanoparticles along the wire sidewall.

split-off hole) can be excited to thermalize and then cooled to the initial state by the phonon emission, within a few picoseconds[25,27,28]. Particularly, the greater part of the thermalized hole is cooled by emission of optical phonons from heavy hole to light hole with a relaxation time of approximately 3 *ps*[28]. Thus, broad frequency spectra are regarded as resulting from a combination of photoexcited electron and hole behavior occurring within picoseconds.

We verified that Au nanoparticles on the sidewall of the Ge NWs assist in promoting THz pulse intensity. To demonstrate the effects of Au nanoparticles, 2D finite difference time-domain (FDTD) simulation was carried out on the Ge NWs with and without Au nanoparticles (**Supplementary Figs. S6 and S7**). The squared contour of $|E/E_0|^2$, where E_0 and E represent the amplitude of the incident and enhanced electric fields, respectively, is shown in Figs. 8a and 8b. The incident light of a 690 nm wavelength is polarized in the y-direction and propagates into the x-direction. The calculated electromagnetic distribution of Ge NWs with Au nanoparticles indicates that enhanced electric fields are locally induced near the Au nanoparticles and expand over the entire wire surface (Fig. 8b), in contrast to Ge NWs without Au nanoparticles (Fig. 8a). Consequently, Au nanoparticles positioned adjacent to each other on the wire surface can enhance THz radiation from the Ge NWs by increasing the strength of the electric field induced there.

Discussion

In summary, cone-shaped Ge NWs were fabricated with Au nanoparticles on the wire sidewall, and a THz pulse emitted from the Ge

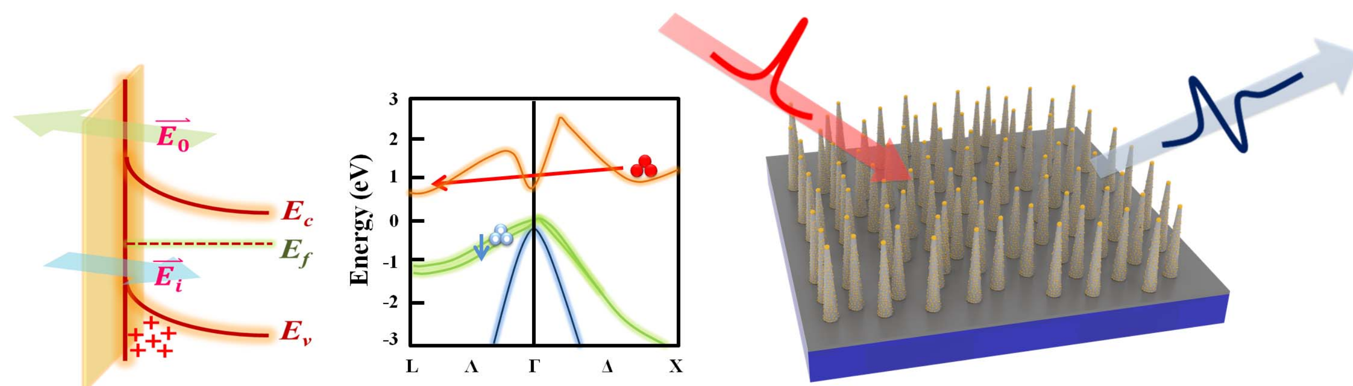

Figure 9 | A schematic diagram of THz generation mechanism in *n*-type Ge NWs by using carrier dynamics of photoexcited e–h in energy band structure.

NWs was observed as a function of wire length. In contrast to the Ge wafer, the Ge NWs could emit strongly enhanced THz pulses for which the THz intensity was greater than with GaAs and even with InAs. Experiments indicate that a critical length of 2.9 μm is necessary to generate the maximum value of Δn. Moreover, the technique of surface modulation by Au nanoparticles is a crucial factor, enhancing THz emissions greater than 2.9 μm by increasing E_b strength in proportion to E_F.

The primary origin of the THz emission from the Ge NWs was attributed to the geometric properties of an extensive surface area to collect photon with multiple paths. Schematically, in n-type Ge, the e–h carriers photoexcited by an *fs* pulse laser are accelerated by the existing built-in electric field ($\overrightarrow{E_0}$), screening the surface field via electron drift into the bulk and hole drift toward the surface, oppositely, which causes dipole oscillations ($\overrightarrow{E_t}$). Simultaneously, photoexcited electrons scattered to the X- and L-valleys in the conduction, and photoexcited holes relaxed to the heavy-light hole band in the valence, and the frequency is consistent with THz, as shown in Fig. 9.

Methods

Synthesizing the Ge NWs. Ge NWs were synthesized by the VLS method using an ultrahigh vacuum CVD system[33,34]. A 2-nm-thick Au film (as a catalyst) was deposited on a cleaned Si (111) substrate in the metal growing chamber at a growth pressure of $\sim 5 \times 10^{-7}$ torr (deposition rate: 0.04 Å/sec) by thermal evaporation. The sample was transferred *in-situ* into the main chamber for annealing at a pressure of $\sim 1 \times 10^{-8}$ torr for 5 min at 400°C, which is the same as the growth temperature, resulting in the formation of Au-Si alloy droplets from the Au film on the Si substrate. After the formation of droplets, Ge NWs were synthesized by filling the main chamber with a mixture of GeH_4 as precursors and H_2 as a carrier gas, with the ratio of GeH_4 to H_2 set from 10 to 50 sccm. A constant total pressure of 2 torr was maintained by a feedback system using a throttle valve and a baratron gauge. To vary the wire length, the total process time was varied from 12 to 80 min, maintaining all other process parameters constant. The morphological characteristics and crystalline structures of Ge NWs were investigated by using field emission scanning electron microscopy (FE-SEM, JSM 6500F, Jeol) and FEI TEM (Tecnai F20) functioning in both the high-resolution transmission electron microscopy (HR-TEM) mode and scanning transmission electron microscopy (STEM) at 200 kV. To investigate the Fermi energy level as a function of wire length and the Au effect, X-ray photoemission spectroscopy (XPS) was employed with Al Kα radiation (PHI-5000 Versaprobe, ULVAC-PHI Inc., Osaka, Japan). The absorbance spectra of the Ge NWs were measured by using an FT-UV-VIS-IR spectrometer (VERTEX 80).

Measurement of radiated THz field. The THz emission from the Ge NWs as a function of wire length was detected using reflection geometry in ambient temperature with a humidity less than 10% in an air-tight box by using custom-built equipment. A Ti:sapphire laser was used as a light source, operating at a pumping wavelength of 790 nm with a repetition rate of 76 MHz and a pulse width of 190 *fs*. The polarization was parallel to the plane of incidence for best pump absorption, using a half-wave plate (HWP). The *fs* laser beam passed through a HWP, after being reflected by mirrors, and was split into a pump beam and a probe beam by a beam splitter (B.S). The pump beam went through a chopper (chopping frequency of 1.7 kHz), while the probe beam was delayed with respect to the pump beam by means of a scanning optical delay line. The pump beam was injected into the sample at an angle of 45° and the pump power used to generate THz radiation was 210 mW. The laser spot size was approximately 3 mm at the surface of the sample. The THz radiation from the sample, in this case for the Ge NWs grown on the Si substrate, was oriented at an angle of incidence of 45° and was collected at an angle of incidence of 45° and focused onto the detector using a pair of parabolic mirrors (PM). The detection antenna was a Hertzian dipole antenna, which had a gap of 5 μm on low-temperature-grown GaAs (LT-GaAs) with a detection bandwidth of 0.2–2.5 THz. The optical power (probe beam) incident on the LTGaAs receiver was 5 mW.

The calculation of the built-in electric field (E_b) at the wire surface in the Ge NWs. Based on the description shown in Fig. 6c, a change in E_F with respect to distance x can induce an electric field at the surface region, which is defined as follows,

$$E_x = -\frac{d\varphi}{dx} = \frac{1}{e}\frac{dE_{Fi}}{dx} \tag{3}$$

where $\varphi = +\frac{1}{e}(E_F - E_{Fi})$.

Assuming quasi-neutral conditions, the surface carrier concentration (n_0) was regarded as a donor impurity concentration (N_d) as expressed by eq. (4) and can be written as eq. (5).

$$n_0 = n_i \exp\left[\frac{E_F - E_{Fi}}{kT}\right] \approx N_d(x) \tag{4}$$

$$E_F - E_{Fi} = kT\ ln\left(\frac{N_d(x)}{n_i}\right) \tag{5}$$

Since the Fermi energy level was constant with distance, it can be differentiated as eq. (6).

$$-\frac{dE_{Fi}}{dx} = \frac{kT}{N_d(x)}\frac{dN_d(x)}{dx} \tag{6}$$

By combining eq. (3) with eq. (6), the electric field was obtained as follows:

$$E_x = -\left(\frac{kT}{e}\right)\frac{1}{Nd(x)}\frac{dN_d(x)}{dx} \tag{7}$$

1. Deibel, J. A., Escarra, M. D. & Mittleman, D. M. Photoconductive terahertz antenna with radial symmetry. *Electronics Letters.* **41** (2005).
2. Lai, R. K., Hwang, J., Norris, T. B. & Whitakera, J. F. A photoconductive, miniature terahertz source. *Appl. Phys. Lett.* **72**, 3100–3102 (1998).
3. Hattori, T., Egawa, K., Ookuma, S. & Itatani, T. Intense terahertz pulses from large-aperture antenna with interdigitated electrodes. *Jpn. J. Appl. Phys.* **45**, L422–L424 (2006).
4. Weiss, C., Wallenstein, R. & Beigang, R. Magnetic-field-enhanced generation of terahertz radiation in semiconductor surfaces. *Appl. Phys. Lett.* **77**, 4160–4162 (2000).
5. Sarukura, N., Ohtake, H., Izumida, S. & Liu, Z. High average-power THz radiation from femtosecond laser-irradiated InAs in a magnetic field and its elliptical polarization characteristics. *J. Appl. Phys.* **84**, 654–656 (1998).
6. Izumida, S., Ono, S., Liu, Z., Ohtake, H. & Sarukura, N. Spectrum control of THz radiation from InAs in a magnetic field by duration and frequency chirp of the excitation pulses. *Appl. Phys. Lett.* **75**, 451–453 (1999).
7. McLaughlin, R. *et al.* Enhanced coherent terahertz emission from indium arsenide in the presence of a magnetic field. *Appl. Phys. Lett.* **76**, 2038–2040 (2000).
8. Heyman, J. N. *et al.* Terahertz emission from GaAs and InAs in a magnetic field. *Phys. Rev. B* **64**, 085202 (2001).
9. Shan, J., Weiss, C., Wallenstein, R., Beigang, R. & Heinz, T. F. Origin of magnetic field enhancement in the generation of terahertz radiation from semiconductor surfaces. *Opt. Lett.* **26**, 849–851 (2001).
10. Vitalij, L. M., Ramunas, A. & Arunas, K. THz emission from semiconductor surfaces. *C. R. Physique* **9**, 130–141 (2008).
11. Johnston, M. B., Whittaker, D. M., Corchia, A., Davies, A. G. & Linfield, E. H. Simulation of terahertz generation at semiconductor surfaces. *Phys. Rev. B* **65**, 165301 (2002).
12. Ahn, H. *et al.* Terahertz emission from vertically aligned InN nanorod arrays. *Appl. Phys. Lett.* **91**, 132108 (2007).
13. Kong, K. J. *et al.* Room-temperature ferromagnetism and terahertz emission of Mn-doped InGaAs and GaAsSb nanowires. *Nanotechnology* **21**, 435703 (2010).
14. Jung, C. S. *et al.* Composition and phase tuned InGaAs alloy nanowires. *J. Phys. Chem. C* **115**, 7843–7850 (2011).
15. Denis, V. S. *et al.* Efficient terahertz emission from InAs nanowires. *Phys. Rev. B* **84**, 115421 (2011).
16. Darmo, J., Strasser, G., Muller, T., Bratschitsch, R. & Unterrainer, K. Surface-modified GaAs terahertz plasmon emitter. *Appl. Phys. Lett.* **81**, 871–873 (2002).
17. Hoyer, P., Theuer, M., Beigang, R. & Kley, E.-B. Terahertz emission from black silicon. *Appl. Phys. Lett.* **93**, 091106 (2008).
18. Jung, G. B. *et al.* Geometry-dependent terahertz emission of silicon nanowires. *Optics Express* **18**, 16353–16359 (2010).
19. Jin, C.-B., Yang, J.-E. & Jo, M.-H. Shape-controlled growth of single-crystalline Ge nanostructures. *Appl. Phys. Lett.* **88**, 193105 (2006).
20. Hemant, A., Ann, F. M., Christopher, E. D. C. & Paul, C. M. Germanium nanowires epitaxy: shape and orientation control. *Nano. Lett.* **6**, 318–323 (2006).
21. Saeta, P. N., Greene, B. I. & Chuang, S. L. Short terahertz pulses from semiconductor surfaces: The importance of bulk difference-frequency mixing, *Appl. Phys. Lett.* **63**, 3482–3484 (1993).
22. Nahata, A., Weling, A. S. & Heinz, T. F. A wideband coherent terahertz spectroscopy system using optical rectification and electro-optic sampling, *Appl. Phys. Lett.* **69**, 2321–2323 (1996).
23. Zhang, X. C. & Xu, J. Introduction to THz wave photonics. DOI: 10.1007/978-1-4419-0978-7_1, Springer Science + Business Media, LLC (2010).
24. Yi, J., Lee, D. H. & Park, W. I. Site-specific design of cone-shaped Si nanowires by exploiting nanoscale surface diffusion for optimal photoabsorption. *Chem. Mater.* **23**, 3902–3906 (2011).
25. Bailey, D. W. & Stanton, C. J. Calculation of femtosecond differential optical transmission in germanium. *J. Appl. Phys.* **77**, 2107–2115 (1995).

26. Roskos, H., Rieck, B., Sellmeier, A. & Kaiser, W. Cooling of a carrier plasma in germanium investigated with subpicosecond infrared pulses. *Appl. Phys. Lett.* **53**, 2406 (1988).
27. Woerner, M., Elsaesser, T. & Kaiser, W. Inter-valence-band scattering and cooling of hot holes in p-type germanim studied by picosecond infrared pulses. *Phys. Rev. B* **41**, 5463 (1990).
28. Tanaka, K., Ohtake, H., Nansei, H. & Suemoto, Tohru. Subpicosecond hot-hole relaxation in germanium studied by time-resolved inter-valence-band Raman scattering. *Phys. Rev. B* **52**, 10709 (1995).
29. Strait, J. H. *et al.* Measurements of the carrier dynamics and terahertz response of oriented germanium nanowires using optical-pump terahertz-probe spectroscopy. *Nano. Lett.* **9**, 2967–2972 (2009).
30. Jacob, H. W., Joshua, B. R., Irene, A. G., Paul, C. M. & Christopher, E. D. C. Vertically oriented germanium nanowires grown from gold colloids on silicon substrates and subsequent gold removal. *Nano. Lett.* **7**, 1637–1642 (2007).
31. Sham, T. K., Yiu, Y. M., Kuhn, M. & Tan, K. H. Electron structure of ordered and disordered Cu_3Au: the behavior of the Au 5*d* bands. *Physical Review B* **41**, 11881–11886 (1990).
32. Bzowski, A., Sham, T. K., Watson, R. E. & Weinert, M. Electron structure of Au and Ag overlayers on Ru(001): the behavior of the noble-metal *d* bands. *Physical Review B* **51**, 9979–9984 (1995).
33. Lee, W. J., Ma, J. W., Bae, J. M., Cho, M. H. & Ahn, J. P. Effects of hydrogen on Au migration and the growth kinetics of Si nanowires. *Cryst Eng Comm.* **13**, 690–696 (2011).
34. Lee, W. J. *et al.* The modulation of $Si_{1-x}Ge_x$ nanowires by correlation of inlet gas ratio with H_2 gas content. *Cryst Eng Comm*, **13**, 5204–5211 (2011).

Acknowledgements

This work was partially supported by the New and Renewable Energy R&D Program (Grant No: 2009T100100614) under the Ministry of Knowledge Economy and Metrology Research Center under Korea Research Institute of Standards and Science. Also, the Yonsei University Research Fund of 2012 for Post doctoral fellowship supported this work.

Author contributions

W.J. Lee performed sample preparation and data analysis. K.S. Jeong and J.S. Wi carried out the FDTD simulations. M.-H. Cho and C. Kang supervised the projects. All authors discussed the results and reviewed this manuscript.

Additional information

Supplementary information accompanies this paper at http://www.nature.com/scientificreports

Competing financial interests: The authors declare no competing financial interests.

How to cite this article: Lee, W.J. *et al.* Strongly Enhanced THz Emission caused by Localized Surface Charges in Semiconducting Germanium Nanowires. *Sci. Rep.* **3**, 1984; DOI:10.1038/srep01984 (2013).

This work is licensed under a Creative Commons Attribution-NonCommercial-NoDerivs Works 3.0 Unported license. To view a copy of this license, visit http://creativecommons.org/licenses/by-nc-nd/3.0